Наносистеми, наноматеріали, нанотехнології
Nanosistemi, Nanomateriali, Nanotehnologii
2024, т. 22, № 3, сс. 535–555
https://doi.org/10.15407/nnn.22.03.535

PACS numbers: 68.37.Lp, 78.55.-m, 87.63.L-, 87.64.Cc, 87.64.km, 87.64.mh, 87.85.jj

Enhanced Efficiency of Samarium-Doped TiO_2 Nanoparticles for Targeted Imaging: Characterization and *in vivo* Evaluation

W. M. Abd El-Kader[1], R. Abo-Gabal[2], A. M. Abdelghany[3], and A. H. Oraby[1]

[1]*Faculty of Science, Physics Department,*
Mansoura University,
Mansoura, Egypt
[2]*Mansoura Urology and Nephrology Centre,*
Mansoura University,
35516 Mansoura, Egypt
[3]*Physics Division, Spectroscopy Department,*
National Research Centre,
33 ElBehouth Str.,
12311 Dokki, Cairo, Egypt

In this study, we synthesize samarium-doped TiO_2 nanoparticles ($Ti(Sm)O_2$ NPs) using solvothermal synthesis and enhance their stability and biocompatibility by coating them with polymeric materials. Extensive characterization studies confirm the desired morphology, crystal structure, optical properties, surface charge, and biocompatibility of the $Ti(Sm)O_2$ NPs. Additionally, *in vivo* imaging evaluations reveal their excellent imaging capabilities, particularly, in distinguishing lung pathologies, making them highly promising for targeted imaging applications. Importantly, *in vivo* toxicity studies demonstrate the biocompatibility and safety of the nanoparticles. These findings contribute to the development of advanced contrast agents for improved diagnostic imaging in biomedical applications, offering potential as effective tools for targeted imaging and enhancing the diagnosis and monitoring of various lung pathologies.

У цьому дослідженні ми синтезуємо леґовані Самарієм наночастинки TiO_2 ($Ti(Sm)O_2$ НЧ) за допомогою сольвотермічної синтези та підвищуємо їхні стабільність і біосумісність шляхом покриття їх полімерними матеріялами. Різноманітні характеризаційні дослідження підтверджують бажану морфологію, кристалічну структуру, оптичні властивості, заряд поверхні та біосумісність $Ti(Sm)O_2$ НЧ. Крім того, оцінки візуалізації *in vivo* показали їхні чудові можливості візуалізації, зокрема у розрізненні патологій легенів, що робить їх дуже перспективними для цільових візуалізаційних застосувань. Важливо, що дослідження токсичности *in vivo* демонструють біосумісність і безпечність наночастинок. Ці висновки сприяють розробці передових контрастних речовин для поліпшеної діягностичної візуалізації в біомедичних застосуваннях, пропонуючи потенційні ефективні інструменти для цілеспрямованої візуалізації та поліпшення діягностики та моніторинґу різних патологій легенів.

Key words: nanoparticles, contrast agents, K-edge, titanium oxide, biocompatibility.

Ключові слова: наночастинки, контрастні речовини, K-край, оксид Титану, біосумісність.

(Received 26 June, 2023; in revised form, 28 June, 2023)

1. INTRODUCTION

The versatility of nanomaterials in performing multiple functions has greatly facilitated their widespread use in the field of cancer imaging, diagnosis, and treatment [1]. Accurate diagnosis of diseases often requires comprehensive information that cannot be obtained through a single imaging modality alone. As a result, multimodal imaging systems have emerged as a promising approach for highly efficient cancer theranostics. In recent years, x-ray computed tomography (CT) has witnessed significant advancements in its core technology and innovative therapeutic applications. However, the development of clinical x-ray contrast agents has seen limited progress in the past few decades. There is a need to overcome challenges such as achieving high concentration in the bloodstream, maintaining stable concentration over time, and enhancing aggregation at specific regions of interest. Addressing these challenges is crucial for improving the performance and efficacy of CT imaging, ultimately advancing the diagnosis and treatment of cancer [2].

The limitations of conventional iodine-based x-ray contrast agents used in CT imaging, such as rapid blood clearance, have prompted the exploration of alternative solutions. In recent years, there has been growing interest in the development of nanoparticle-based contrast agents to address these limitations [3]. Nanoparticulate probes offer several advantages over single molecule-based agents, including the ability to integrate different contrast-generating materials, longer circulation time in the bloodstream, and higher payload capacity. This review highlights the significance of nanoparticle-based contrast agents in medical imaging, particularly in the context of CT imaging, and their potential to enhance imaging performance and capabilities [4]. By leveraging the unique properties of nanoparticles (NPs), researchers aim to overcome the challenges associated with conventional contrast agents and improve the accuracy and quality of CT imaging for various medical applications.

Gold nanoparticles (AuNPs) show promise as iodine-free x-ray contrast agents in medical applications [5]. Gold unique properties, including its higher nuclear number, K-edge, and mass x-ray absorption coefficient compared to iodine, make it an attractive alternative. AuNPs provide 2.7 times greater x-ray contrast per unit weight than iodine and exhibit optimal x-ray absorption in the 80–100 keV range, enabling improved visualization of blood vessels [6]. Moreover, AuNPs have demonstrated excellent biocompatibility and low toxicity, rendering them suitable for a range of biological applications [7].

Bismuth (Bi), a metal with a high nuclear number ($Z_{\mathrm{Bi}} = 83$), has gained interest as a potential alternative to iodine-based x-ray contrast agents due to its low toxicity and diverse applications in medicine, cosmetics, and surgery. Bismuth salts were among the earliest contrast agents used in x-ray imaging of patients [8]. Coated bismuth NPs were introduced as injectable contrast agents for CT imaging in mice, demonstrating prolonged circulation compared to iodine-based agents [9]. Bismuth-enhanced nanocolloids have also been utilized as contrast agents for spectral CT molecular imaging to visualize thrombus [10]. However, due to their high cost and adverse effects, high doses of bismuth compounds were eventually replaced by more cost-effective alternatives. This review highlights the potential of bismuth as an x-ray contrast agent, its early applications, and the challenges in its widespread use.

In the early 1970s, tantalum NPs were investigated as a contrast agent for bronchography. However, compared to iodine, tantalum had a limited contrast impact, especially at high x-ray voltages [11]. *In vivo* studies in mice demonstrated the absence of immediate or harmful effects, and the NPs were eliminated through renal clearance without adverse effects. More recently, Hyeon *et al.* developed a microemulsion strategy to synthesize uniform-sized TaO_x particles in large quantities, opening up new possibilities for their application as contrast agents. This review highlights the historical usage of tantalum NPs in bronchography, their contrast properties, and the latest advancements in their synthesis for potential medical imaging applications [12].

Lanthanide elements, such as gadolinium and ytterbium, have shown significant potential for use in x-ray scanning techniques. These elements possess higher nuclear numbers than iodine, resulting in increased x-ray attenuation and enhanced contrast in polyspectrum imaging. Gadolinium, in particular, exhibits a higher K-edge (52 keV) compared to iodine, leading to more pronounced x-ray attenuation and superior contrast. Ytterbium, among the lanthanide elements, stands out as a promising candidate for diagnostic and molecular imaging applications due to its excellent biocompatibility and high mass x-ray absorption coefficient [8]. Among the lanthanide elements, ytterbium is the most promising contender for diagnostic and molecular imaging applications due to its excellent biocompatibility and high mass x-ray absorption coefficient ($3.88\ \mathrm{cm^2 \cdot g^{-1}}$ at 100 keV) [13].

Titanium dioxide (TiO_2) NPs have gained significant attention as a semiconductor material due to their high photochemical stability and cost-effectiveness [14]. To optimize their radiosensitizing effects, doping TiO_2 NPs with high Z-elements while preserving their fundamental physical properties was explored [15]. In this regard, the incorporation of samarium (Sm) into TiO_2 NPs has been investigated, resulting in enhanced efficiency. These $Ti(Sm)O_2$ NPs immobilized with polyethylene glycol (PEG) and fluorescent dye offer a multifunctional platform for x-ray computed tomography (CT) and fluorescence imaging. Notably, $Ti(Sm)O_2$ NPs exhibit desirable characteristics such as biocompatibility, antimicrobial properties, high chemical stability, specific surface area, and catalytic activity. This review highlights the potential of $Ti(Sm)O_2$ NPs and their unique properties for various biomedical applications, including imaging and therapeutic interventions [2].

The surface characteristics of NPs play a crucial role in their biomedical applications, influencing their interactions within the human body. Coatings on NPs can provide protection against mononuclear phagocyte and protein adsorption *in vivo*, thereby, maintaining their stability. However, creating a surface coating material that offers colloidal stability and biocompatibility under physiological conditions is a significant challenge [16]. The choice of coating agent and its interaction with the biological environment determine the stability and biocompatibility of NPs [17]. Different classes of coating substances, such as synthetic and natural hydrophilic polymers like poly(ethylene glycol) (PEG), poly(vinyl alcohol) (PVA), and poly(L-lysine) (PLL), have been investigated for their potential in biomedical applications [18, 19]. These coatings have shown benefits such as enhanced colloidal stability, reduced cytotoxicity, and improved biocompatibility of various NPs, including iron oxide and titanium dioxide NPs [20]. One common class of compounds are synthetic and natural hydrophilic polymers such as poly(ethylene glycol) (PEG) which modified USPIONs synthesized [20], and poly(vinyl alcohol) (PVA), which shows superparamagnetic, hydrophilic properties and may serve as a potential candidate for biomedical applications [21], poly(L-lysine) (PLL) which provide good colloidal stability for iron oxide and modified NPs less than 10 nm in diameter were tested for cell labelling [22].

Mano *et al.* found that modifying TiO_2 NPs with PEG reduces their cytotoxicity and the induction of stress-related genes [23]. This study aims to enhance the imaging capabilities of titanium dioxide (TiO_2) NPs by incorporating lanthanides and improving their physical and biological properties. By coating these NPs with polymers, they can be used as safe and biocompatible x-ray computed tomography (CT) contrast agents *in vivo*. The findings of this study demonstrate the potential applications of lanthanide-doped TiO_2 NPs and other multifunctional NPs in cancer diagnostics and therapy. These results underscore the importance of harnessing the unique properties of lanthanide-doped TiO_2 NPs for advanced imaging techniques and their potential significance in cancer research and treatment.

2. MATERIALS AND METHODS

2.1. Materials

Titanium dioxide (TiO_2 = 79.89 g, min. assay (*ex* Ti) 99%, max. limits of impurities, loss on drying 5%, iron (Fe) 05%). Sodium hydroxide (sodium hydroxide pellets AR assay 99.5%, MW.40.00, SO. 55592, Egypt). Carboxymethyl (CMC), carmellose sodium, assay: 99.5% pure Na–CMC, maximum 5 salts, PH: 6.5:8.5, density: 1.59 g/cm^3, soluble in water, loss on drying max. 10%. Polyvinyl pyrrolidone (PVP), (K-30), pure, M.W. = 40000, Mumbai, India. Polyethylene glycol 6000 (PEG 6000), molecular mass: 40.3 g/cm^3, soluble in water, density: 3.58 g/cm^3. Samarium (III) nitrate hexahydrate, 99.9% (REO), hygroscopic, store under nitrogen, 10 g, LOT: D12X008, FW: 444.45, Germany. All the aqueous solutions are prepared using triple distilled deionized water (DW).

2.2. Synthesis of TiO_2 NPs

TiO_2 NPs were synthesized using the hydrothermal method. Initially, a solvent mixture was prepared by combining 5 g of TiO_2 and 4.8 g of NaOH in 60 ml of deionized water at room temperature. The mixture was stirred for 3 hours at 60°C, resulting in a clear solution. To achieve a pH of 7, filtration using filter papers was performed. The solution was then dried at 60°C.

The dried solution was magnetically stirred and transferred to a 100 ml teflon-lined stainless steel autoclave, which was heated to 150°C for 3 hours. After cooling to room temperature, the obtained product was washed five times with pure ethyl alcohol and distilled water. The resulting white precipitate was dried overnight at 60°C and subsequently calcined at 500°C for 2 hours.

2.3. Synthesis of 1% Sm-Doped TiO_2 NPs ($Ti(Sm)O_2$ NPs)

To synthesize the $Ti(Sm)O_2$ NPs, samarium (III) nitrate hexahydrate was added to the mixture. Following the hydrothermal method mentioned earlier, the preparation involved the use of ethanol, HCl, and deionized water. Specifically, a solution was created by mixing 30 ml of ethanol, 0.5 ml of HCl, 2 ml of deionized water, and 1% samarium. Under stirring, 5 ml of titanium oxides were added drop by drop to the solution and vigorously stirred for 15 minutes, following the same procedure as described previously.

2.4. Synthesis of Polymer Encapsulated TiO_2 and Sm-Doped TiO_2 NPs

To enhance the stability of the CT contrast agents, we implemented three surface modifications on the NPs. The NPs were designed with a core-shell structure, where the NP core comprised multiple CT-dense nanocrystals (NCs), and the shell was formed using FDA-approved polymers: polyethylene glycol (PEG), polyvinylpyrrolidone (PVP), and carboxymethyl cellulose (CMC). To carry out the surface modification, a solution containing 0.1 g of TiO_2 NPs and 0.1 g of each polymer (PEG, PVP, and CMC) was mixed in 100 ml of deionized water. The mixture was then stirred at 60°C for 3 hours. Subsequently, the solutions were separated through centrifugation at 60 rpm for 2 minutes, and the resulting NPs were dried at 60°C.

2.5. Characterization Techniques

The optical properties of the synthesized NPs were characterized using a UV–Vis spectrometer (Pg instruments, T_{80}^{+}, UV/Vis spectrometer, China). Absorbance spectra measurements were performed in the wavelength range of 200–900 nm to investigate the optical properties of the NPs. This range encompasses the UV, visible, and near-infrared regions of the electromagnetic spectrum, where electronic transitions occur. Molecules with bonding and non-bonding electrons (n-electrons) can absorb energy from ultraviolet or visible light, causing them to be excited to higher antibonding molecular orbitals. The UV–Vis spectroscopy provides valuable insights into the electronic transitions and optical behaviour of the NPs [24].

The functional groups present in the synthesized TiO_2 NPs were identified using Fourier transform infrared (FTIR) spectroscopy. The FTIR spectra were collected using an FTIR spectrophotometer (PerkinElmer-99075, Germany) employing the standard KBr pellet technique. The spectral range analysed was 4000–450 cm^{-1}, with a resolution accuracy of 4 cm^{-1} FTIR spectroscopy is a powerful technique that enables the characterization and identification of various functional groups present in the NPs, providing valuable information about the chemical composition and structure of the synthesized TiO_2 NPs.

Transmission electron microscopy (TEM) imaging was performed using a JEOL JEM-2100 instrument from Japan, equipped with a CCD camera. To prepare the samples for TEM measurements, a wax plate was covered with a copper grid, and a diluted nanosuspension was sprayed onto the surface of the grid [25]. This ensured that the nanostructures formed in the colloids were visualized under the TEM. The obtained TEM images provided high-resolution details of the NPs and their morphology.

Additionally, the size distribution of the NPs was analysed using ImageJ 64-bit software (version ij 153-win-java 8), and a size distribution histogram was generated to estimate the particle size range and distribution.

The zeta potential of the NPs was determined using a zeta potential analyser and particle sizing devices at a temperature of 25 degrees Celsius. The specific instrument used for this analysis was the Malvern Zetasize Nano-zs 90 from the U.S.A. The zeta potential measurement provides information about the surface charge of the NPs. When particles have a high negative or positive zeta potential, they tend to repel each other, leading to a stable colloidal suspension with no flocculation. Conversely, particles with low zeta potential values lack the repulsive force necessary to prevent their collision and flocculation. According to the principle of electrophoresis, NPs with zeta potentials exceeding +30 mV or falling below −30 mV are considered to be colloidal and exhibit stability (Franks, 2002). The zeta potential analysis helps assess the stability of the NPs and their potential for aggregation or dispersion in solution [26].

Luminescence qualities were assessed using a spectrofluorometer (Jasco FP-6500, Japan) and two-photon laser confocal microscopy (690–1040 nm) (Xenon arc Lamp 150 watt). The excitation and emission spectra were used to analyse the nanocomposites' luminescence capabilities. Before measurement, the nanocomposite is purified by dialysis against distilled water for one week, and the purified samples are distributed in distilled water [19].

2.6. Cytotoxicity and Cell Viability Assay

In the cytotoxicity and cell viability assay, peripheral mononuclear cells (PBMC) were isolated from whole blood using density centrifugation with Ficoll–Paque. The procedure involved centrifuging Hanks balanced salt solution (HBSS) with heparinized human blood, collecting the upper fraction containing PBMCs, and resuspending the cells in PBS buffer. Cell counting was performed using a haemocytometer and the trypan blue exclusion method. The isolated PBMCs were then seeded in a 96-well plate with a culture medium and incubated at 37°C with 5% CO_2.

For cell characterization, PBMCs at passage three were analysed by flow cytometry using anti-CD45 PE antibody [27]. The cells were stained, and data analysis was performed using a flow cytometer. To assess cell viability and cytotoxicity of the NPs, cells were seeded in a 96-well plate and incubated with the NPs for a specific duration. After incubation, trypan blue was added to each well, and the plates were further incubated and placed on a shaker to facilitate cell–NP interaction. Cell morphology was assessed by capturing photographs of living cells' interaction with different NPs. These experimental procedures, as described by Gabal *et al.* (2022), allowed for the evaluation of cytotoxicity and cell viability using peripheral mononuclear cells. The isolation and characterization of PBMCs provided a standardized cell population for the assessment, and the incubation with NPs allowed for the observation of any potential effects on cell viability and morphology [28].

2.7. Assessment of the Toxicity and Safety Profile

The study was conducted on 51 male mice weighing 29–40 g. They were obtained from the animal house of MERC, the faculty of medicine, Mansoura University, and after approval by our local ethical committee. Considering that accumulation of NPs *in vivo* might stimulate toxicity or adverse side effects after long-term treatment, we next evaluated the potential long-term toxicity of NPs *in vivo*.

Animal Model. The mice were randomly allocated into two groups (24 rats each) and three control. The control group was injected with saline only; after intravenous injection (IV) of NPs, mice were sacrificed after 3 hrs and 7 days, major organs (liver, heart, lung, spleen, pancreas, and kidneys) were collected for H&E staining. Samples were then fixed in 10% formalin, followed by routine dehydration, immersion, and paraffin embedding. They were sectioned into 4-μm-thick slices for haematoxylin and eosin staining and examined by light microscopy.

Degenerative changes were observed and graded into: absent, defined as no obvious pathological changes; mild, defined as focal pathological changes; or marked, defined as diffuse pathological changes, as modified from a previous report. Blood biochemistry analyses were performed, and blood samples were also collected to investigate nephrotoxicity and hepatotoxicity. Aspartate aminotransferase, alanine aminotransferase, and creatinine levels were determined after 1 hr and 6 days of treatment in serum samples collected. Levels of ALT and AST refer to liver damage. A measurement of the serum creatinine level is often used to evaluate kidney function.

2.8. *In vitro* Phantom Imaging

For *in vitro* phantom measurements, solutions of TiO_2 and samarium-doped TiO_2 were prepared at various concentrations 6.25, 12.5, 25.0, 50.0, and 100.0 mM diluted in DW in 1.0 ml microtubes. Phantom CT images were acquired on a Toshiba Alexion CT scanner operating at 80, 100, 120 keV, and 22, 30, 37 μA, respectively, with a slice thickness of 0.5 mm and gantry rotation time of 0.6 s. Images were analysed using J-image 64-bit (ij 153-win-java 8). Create a circular region of interest (ROI) over each tube, and the attenuation and standard deviation were recorded for each ROI analysed [29]. From these values, the Contrast rates were calculated for different image sets *via* the equation

$$\text{Contrast} = (I_{\max} + I_{\min})/(I_{\max} - I_{\min}).$$

3. RESULTS AND DISCUSSION

3.1. UV/Visible Optical Absorption Spectral Data

The study involved recording ultraviolet–visible (UV/Vis) absorbance spectra to evaluate the electronic structure and optical band gap of the NPs. The UV/Vis spectra of pure titanium dioxide (TiO_2) NPs and samarium-doped TiO_2 NPs were obtained and analysed.

In Figure 1, *a*, the absorbance peak at 364.23 nm corresponds to the presence of TiO_2 in the sample. In Figure 1, *b*, two absorption peaks are observed for samarium-doped TiO_2 at 366.65 nm and 409.2 nm, with the latter attributed to the presence of samarium. The specific absorption characteristics may vary with different polymeric precursors used in the synthesis process. The absorption edge in the UV region represents electronic transitions from the occupied valence band to the empty conduction band. Absorption occurs when the energy of the incident

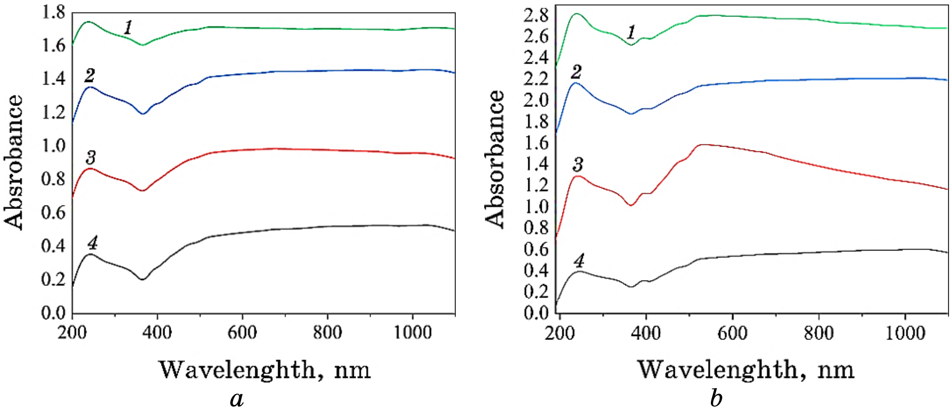

a *b*

Fig. 1. (*a*) UV spectra of: *1*—TiO_2, *2*—PVP@TiO_2, *3*—PEG@TiO_2, and *4*—CMC@TiO_2 NPs; (*b*) UV spectra of: *1*—$Ti(Sm)O_2$, *2*—PVP@$Ti(Sm)O_2$, *3*—PEG@$Ti(Sm)O_2$, and *4*—CMC@$Ti(Sm)O_2$ NPs.

photon matches or exceeds the band gap energy of the material.

3.2. FTIR Analysis

Infrared spectroscopy (FTIR) was employed to analyse the functional groups present in the synthesized compounds. Figure 2 illustrates a series of FTIR spectra for TiO_2 and samarium-doped TiO_2 NPs, coated with PVA, PEG, and CMC. In the spectra, a prominent and strong band in the range of 580–660 cm^{-1} corresponds to the characteristic modes of TiO_2. This band provides evidence of the presence of TiO_2 in the samples. Additionally, an absorption range around 3427 cm^{-1} indicates the stretching vibrations of hydroxyl groups, which may be influenced by in-situ spectra recording and water reabsorption from the ambient atmosphere. Another absorption range around 1553 cm^{-1} is attributed to the bending vibrations of hydroxyl groups in molecular water. The bands in the range of 1000–400 cm^{-1} are associated with the Ti–O modes, further confirming the presence of TiO_2.

Furthermore, the FTIR spectrum of the coated TiO_2 NPs is presented in Fig. 2 too. The absorbance observed in the range of 1066–1700 cm^{-1} corresponds to the vibrations of organic polymers. The appearance of new bands in this region is attributed to the existence of the organic polymer coating. For example, bands around 2881, 1352, and 1066 cm^{-1} represent the stretching vibrations of C–H bonds, the bending vibrations of C–H bonds, and the stretching vibrations of C–O bonds, respectively. The presence of these bands indicates the hydrogen-bonding nature and confirms the interaction between the organic polymer and the surface of TiO_2 and samarium-doped TiO_2 NPs. This interaction between the polymers and the NPs further supports the

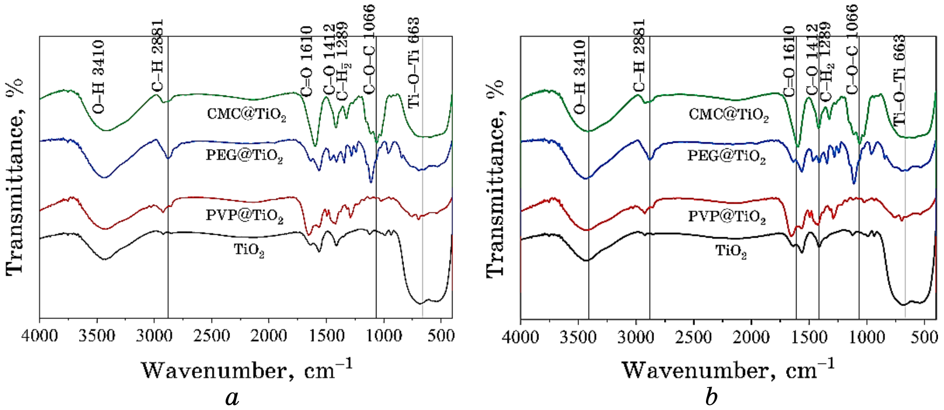

a *b*

Fig. 2. FTIR spectra of: (*a*) PVP@TiO_2, PEG@ TiO_2, CMC@ TiO_2 NPs; (*b*) $Ti(Sm)O_2$, PVP $Ti(Sm)O_2$, PEG @$Ti(Sm)O_2$, CMC @$Ti(Sm)O_2$ NPs.

successful coating process and provides valuable information about the surface chemistry of the synthesized NPs.

3.3. Zeta Potential

The ζ-potential values of prepared NPs sintered are shown in Fig. 3. ζ-potential has been utilized to be aware of the nature of prepared nano-

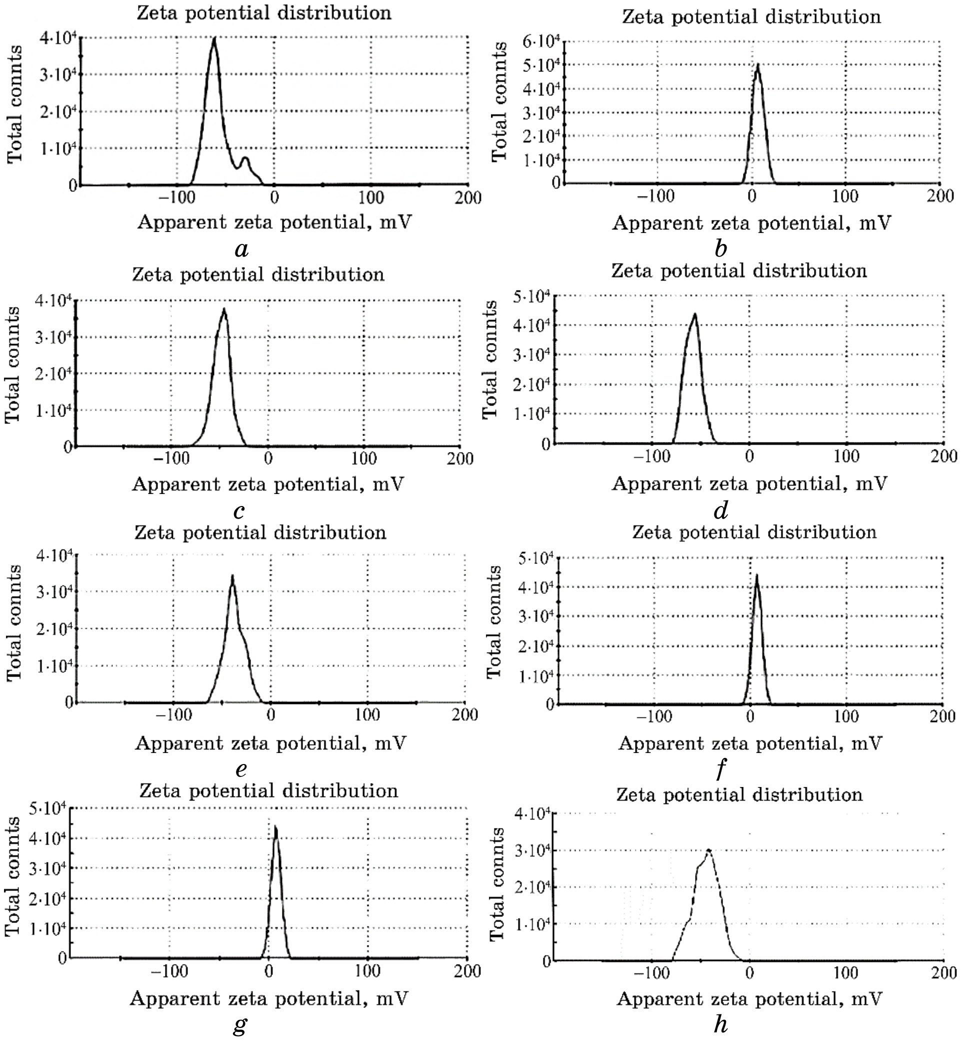

Fig. 3. Zeta potential for NPs: (*a*) TiO_2; (*b*) PVP@ TiO_2; (*c*) PEG@ TiO_2; (*d*) CMC@TiO_2; (*e*) Ti(Sm)O_2; (*f*) PVP@Ti(Sm)O_2; (*g*) PEG@Ti(Sm)O_2; (*h*) CMC@Ti(Sm)O_2.

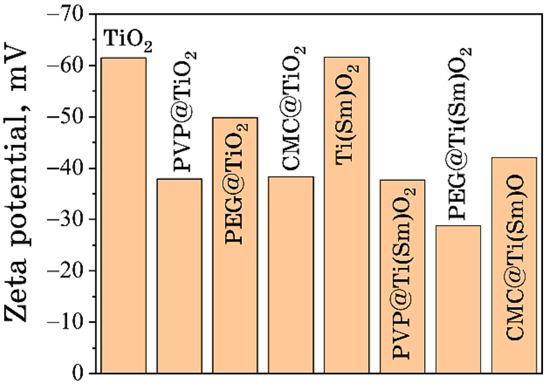

Fig. 4. Zeta potential distribution of TiO_2, PVP@TiO_2, PEG@TiO_2, CMC@TiO_2, Ti(Sm)O_2, PVP@Ti(Sm)O_2, PEG@Ti(Sm)O_2, and CMC@Ti(Sm)O_2 NPs.

particle charges in DW. ζ-potential with a negative value ranging from –37.7 mV to –61.5 mV was obtained for the nanoparticle diluted in DW, corresponding to a stable colloidal without particle settlement. ζ-potential lowered as the NPs was coated with polymers, as in Fig. 4. Moreover, the prepared suspension endorsed with general ζ-potential value of 30 mV with a positive or negative sign for better stability. Lower values of ζ-potential suggest aggregation of NPs due to van der Waals forces. Zhang *et al.* confirmed the measurement of the ζ-potential of the material to understand the nature of cellular interaction, cellular diagnostics, and therapeutics of normal and cancer cell effects.

3.4. Transmission Electron Microscopy (TEM) and Photoluminescence

TEM of TiO_2, Ti(SmO_2) NPs declared a spherical morphology and a comparably narrow size dispersion characteristic of the hydrothermal method.

The particle-size distribution histogram was outlined regarded the counted ten NPs as shown in Fig. 5. The mean particle size is of 80 nm with a 23.59 nm standard deviation. The particle-size distribution histogram was outlined regarded to the counted ten NPs. The mean particle size of Ti(SmO_2) is 83 nm with a 22.30 nm standard deviation.

As an indirect band gap semiconductor, TiO_2 shows no band gap photoluminescence. Photoluminescence (PL) arises from recombining oppositely charged trapped and free carriers. Photoluminescence from Ti(Sm)O_2 suspension contains a band at 600 nm and a band at around 515 nm. The band at 600 nm exhibits a strong correlation with defects, and the 515 nm band shows a close relationship with the oxygen vacancies.

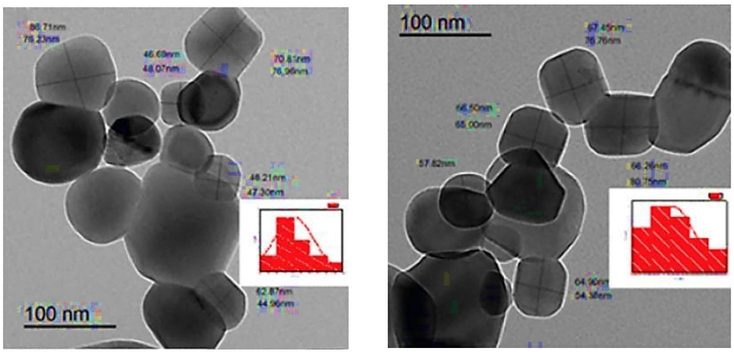

a *b*

Fig. 5. (*a*) TEM of TiO_2 NPs and the corresponding particle size distribution histogram; (*b*) TEM of $Ti(Sm)O_2$ and the corresponding particle-size distribution histogram.

A series of $Ti(Sm)O_2$ PL studies in different coated samples in Fig. 6. The normal emission of NPs is dominated by PL arising from the recombination of trapped electrons with valence band holes, leading to a broad spectrum with a peak in 600 nm. In addition, it is presented a higher energy emission from recombining mobile electrons with trapped holes. Because both types of recombination depend on the spatial coincidence of trapped and roaming charges, comparing the energy

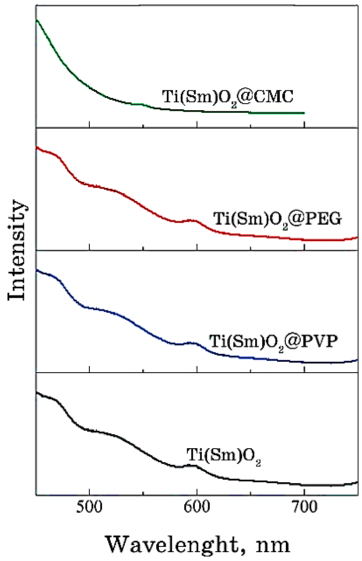

Fig. 6. Photoluminescence of $Ti(Sm)O_2$, PVP@$Ti(Sm)O_2$, PEG@$Ti(Sm)O_2$, and CMC@$Ti(Sm)O_2$ NPs.

TABLE 1. Characterization of TiO_2 NPs.

Sample	Zeta potential, mv	Conductivity, ms/cm	Energy gap, eV	Particle size, nm
TiO_2	−61.5	3.16	3.4	70.5
PVP@TiO_2	−37.9	0.99	2.95	
PEG@TiO_2	−49.8	2.2	2.99	
CMC@TiO_2	−38.27	2.2	2.88	
Ti(Sm)O_2	−61.6	2.5	2.97	83.03
PVP@Ti(Sm)O_2	−37.7	3.02	2.9	
PEG@Ti(Sm)O_2	−28.8	1.56	2.7	
CMC@Ti(Sm)O_2	−42.6	4.08	2.8	

gaps and conductivity values (Table 1) with PL (Fig. 6) obtained from prepared samples, we can conclude that the PL intensity is greater when transport is hindered and lower when the charges are more mobile. As shown in Table 1, the PL peaks diminishes in CMC@Ti(Sm)O_2 with more conductivity value and less energy gap.

3.5. Phenotypic Characterization of PBMCs

In passage three, PBMCs were characterized using flow cytometric analysis. The results showed that PBMC cells positively express hematopoietic markers CD45 (70.9% ; Fig. 7).

3.6. Human Mononuclear Cell Culture and Treatment Protocol

The morphological microstructure (×100) is observed using an Olympus IX51inverted fluorescence microscope.

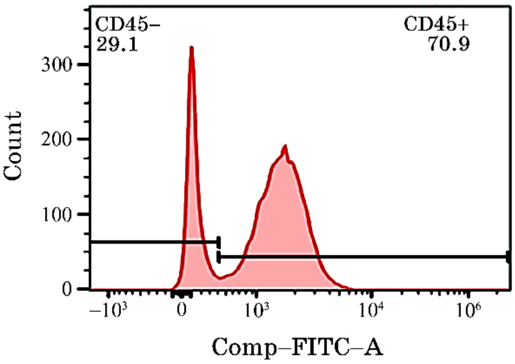

Fig. 7. CD 45 FTIC mouse antihuman (561865, BD).

Recording the viability for each plate after 90 min, as shown in Fig. 8, shows the viability for the mononuclear cells after incubation with NPs in the dilatation (1NPs:1cells), (1NPs:3cells), (1NP_s:5cells). Cell viability results ensure TiO_2, PVP@TiO_2, PEG@TiO_2, CMC@TiO_2, Ti(Sm)O_2, PVP@Ti(Sm)O_2, PEG@Ti(Sm)O_2, and CMC@Ti(Sm)O_2 NPs is blood biocompatibility; so, it will be completely safe within few hours before any interaction with blood cells occurs. The blood biocom-

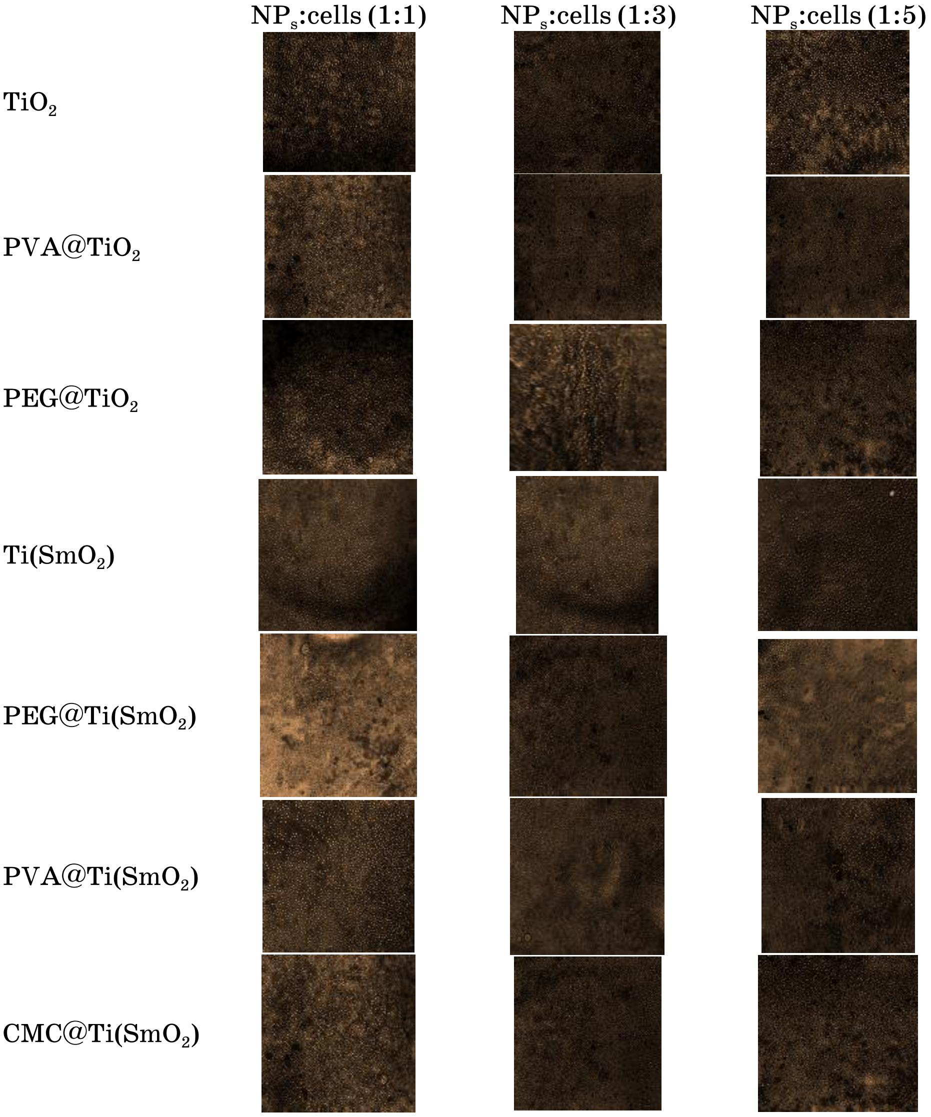

Fig. 8. The mononuclear cells after incubation with NPs after 90 min.

patibility of our synthesized NPs may relate to its surface nature.

After injecting a dose of NPs (0.1 ml), rats were dissected and subjected to haematoxylin and eosin (H&E) examination at 1 hour and 6 days post-injection. The H&E examination results at 1 hour showed that most of the NPs accumulated in the lung. However, no adverse effects of the NPs were observed in the pancreas, heart, lung, or kidney. Nonetheless, variable levels of injuries were observed in the lung, liver, and heart, depending on the nature of the injected NPs. In the lung samples taken after 1 hour, diffuse alveolar damage (DAD) was observed.

DAD is characterized by congested lung vessels, interstitial haemorrhage and fibrosis, interstitial neutrophils, bloody exudates in the alveoli, pulmonary congestion, bronchiolar epithelial damage, and hemosiderin-laden macrophages. In the liver, mild portal inflammation and little bile duct proliferation were observed in samples injected with NPs, except for TiO_2 coated with PVA, which showed minimal portal inflammation and no bile duct proliferation. Hepatocyte degeneration (pyknotic) was observed in zone 1, 2, and 3 of the liver for TiO_2. TiO_2@CMC and $Ti(SmO)_2$@PVA exhibited hepatocyte degeneration and injury in zone 2 and 3. TiO_2@PVA and $Ti(SmO)_2$ showed hepatocyte degeneration and injury in zone 3. TiO_2 coated with PEG showed scattered spotty necrosis in hepatocytes in zone 3. However, no hepatocyte injury was found in $Ti(SmO)_2$@PEG and $Ti(SmO)_2$@CMC.

To assess the long-term toxicity of the NPs, histological examination was conducted on several organs, including the heart, liver, lung, pancreas, kidney, and spleen after seven days (see Fig. 9). H&E examination revealed no adverse effects of the NPs on the heart, pancreas, kidney, and spleen. Fortunately, the lung showed complete resolution for TiO_2, PEG@TiO_2, CMC@TiO_2, $Ti(Sm)O_2$, PVP@$Ti(Sm)O_2$ NPs.

Serum levels of alanine aminotransferase (ALT), aspartate aminotransferase (AST), and creatinine (Cr) were measured after 1 hour and seven days to evaluate liver and kidney function (Table 2). After 1 hour, ALT levels indicated minimal liver toxicity, while creatinine levels indicated normal kidney function. However, AST levels were higher. After seven days, ALT and AST levels indicated minimal liver toxicity, and creatinine levels indicated normal kidney function.

Based on the biodistribution of TiO_2 NPs, they can potentially be developed as target-specific agents for lung-related pathologies, allowing for the selective distinction of lung diseases.

X-ray CT phantom images were captured using various concentrations of TiO_2 and $Ti(Sm)O_2$ coated with various polymers diluted with distilled water (Fig. 10).

The CT number increased as the concentration of NPs increased (Fig. 11); the variation, in contrast, is slightly varied. However, the high contrast was gained at 80 keV.

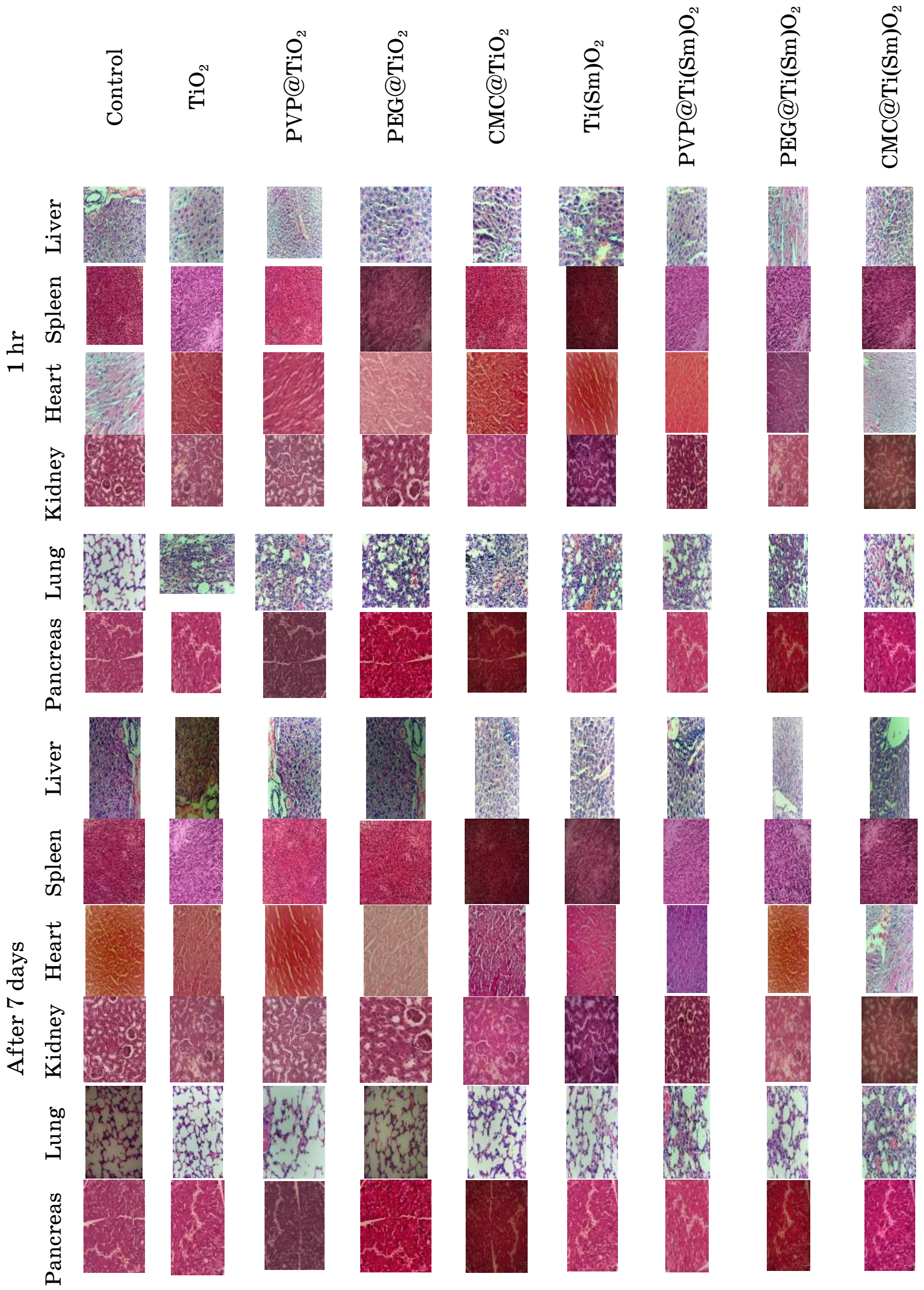

Fig. 9. Histological examination of heart, liver, lung, pancreas, kidney, and spleen injected by 0.1 ml saline and NPs followed by dissection after 1 hr and 7 days, sections were stained with H&E and observed under the light microscope at 400× magnification.

TABLE 2. Toxicological effect on serum levels of ALT, AST, and creatinine.

After 1 h	Creatinine, U/L	ALT, U/L	AST, U/L
Control	0.15	22	110
TiO_2	0.27	47	516
$PVP@TiO_2$	0.29	57	671
$PEG@TiO_2$	0.26	39	310
$CMC@TiO_2$	0.25	45	305
$Ti(Sm)O_2$	0.25	40	480
$PVP@Ti(Sm)O_2$	0.24	56	620
$PEG@Ti(Sm)O_2$	0.23	63	588
$CMC@Ti(Sm)O_2$	0.24	50	638
After 7 days			
TiO_2	0.25	30	220
$PVP@TiO_2$	0.28	26	229
$PEG@TiO_2$	0.24	24	145
$CMC@TiO_2$	0.23	24	130
$Ti(Sm)O_2$	0.24	28	163
$PVP@Ti(Sm)O_2$	0.23	30	177
$PEG@Ti(Sm)O_2$	0.24	29	176
$CMC@Ti(Sm)O_2$	0.16	23	260

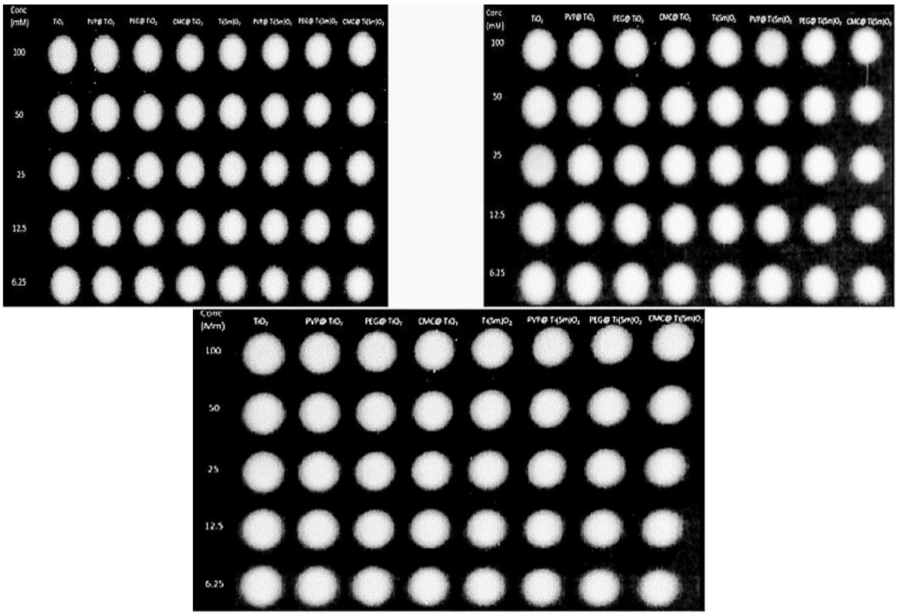

Fig. 10. CT phantom images of TiO_2, $PVP@TiO_2$, $PEG@TiO_2$, and $CMC@TiO_2$ NPs by UV spectra of $Ti(Sm)O_2$, $PVP@Ti(Sm)O_2$, $PEG@Ti(Sm)O_2$, and $CMC@Ti(Sm)O_2$ NPs.

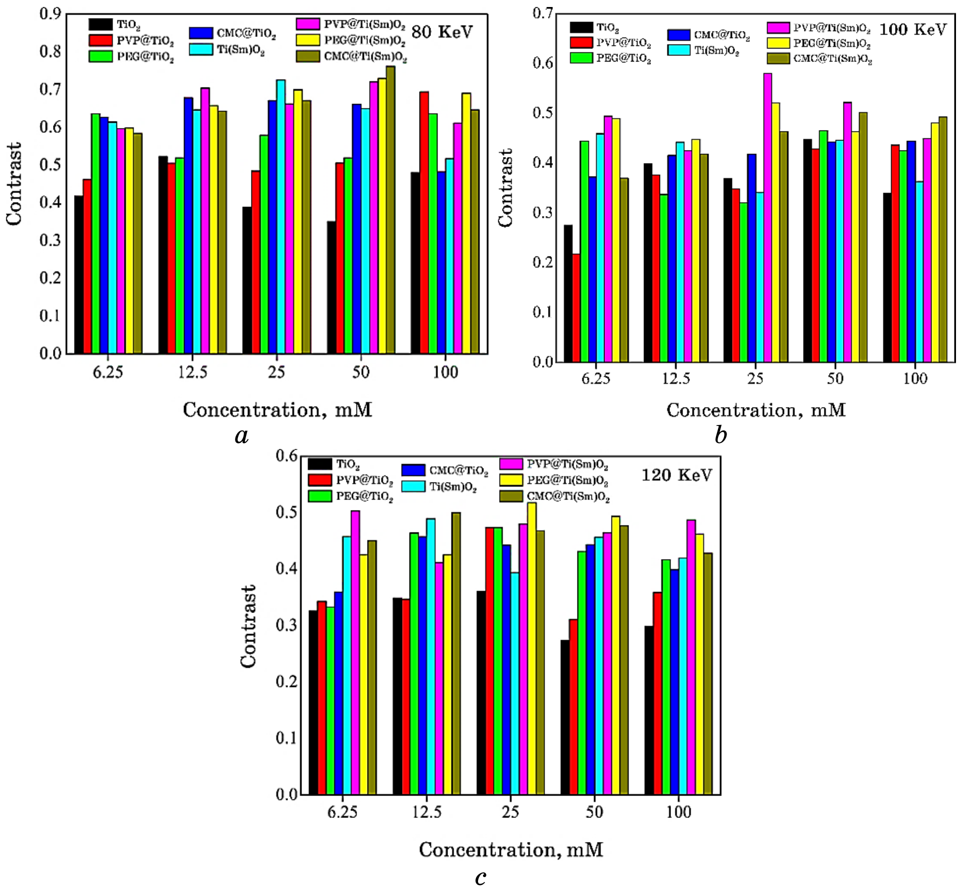

a *b* *c*

Fig. 11. Contrast of TiO$_2$, Ti(SmO$_2$) coated with PEG, CMC, PVP: (*a*) 80 keV; (*b*) 100 keV; (*c*) 120 keV.

4. CONCLUSION

The synthesized TiO$_2$ and Ti(Sm)O$_2$ NPs coated with PVA, PEG, and CMC have shown promising characteristics for use as CT scan contrast agents. These NPs exhibit small size, high stability, high contrast, long blood retention time, and low toxicity. Both *in vitro* and *in vivo* toxicity assessments have demonstrated their excellent biocompatibility and low risk of adverse effects. Furthermore, the imaging performance of these NPs in CT scans has been found to be superior. They exhibit higher x-ray absorption coefficients and longer blood circulation time, making them effective contrast agents for CT imaging. The incorporation of samarium doping in TiO$_2$ NPs has further enhanced their performance in fluorescent imaging, making them suitable for dual imaging applications. Based on these findings, the synthesized TiO_2 and $Ti(Sm)O_2$ NPs coated with PVA, PEG, and CMC hold significant potential for clinical applications in dual imaging. Their unique properties and biocompatibility make them promising candidates for improving the accuracy and effectiveness of CT imaging in medical diagnostics.

ETHICS APPROVAL AND CONSENT TO PARTICIPATE

Animal studies were performed in MERC accredited facility under the approval of Faculty of Medicine, Mansoura University.

REFERENCES

1. K. H. Bae, H. J. Chung, and T. G. Park, *Mol. Cells*, **31**, Iss. 4: 295 (2011); doi:0.1007/s10059-011-0051-5
2. F. Hallouard, N. Anton, P. Choquet, A. Constantinesco, and T. Vandamme, *Biomaterials*, **31**, Iss. 24: 6249 (2010); doi:10.1016/j.biomaterials.2010.04.066
3. Y. Liu, K. Ai, and L. Lu, *Accounts of Chemical Research*, **45**, Iss. 10: 1817 (2012); doi:10.1021/ar300150c
4. D. P. Cormode, P. C. Naha, and Z. A. Fayad, *Contrast Media Mol. Imaging*, **9**, No. 1: 37 (2014); doi:10.1002/cmmi.1551
5. J. F. Hainfeld, D. N. Slatkin, T. M. Focella, and H. M. Smilowitz, *Br. J. Radiol.*, **79**, No. 939: 248 (2006); doi:10.1259/bjr/13169882
6. P. A. Jackson, W. N. Rahman, C. J. Wong, T. Ackerly, and M. Geso, *European Journal of Radiology*, **75**, No. 1: 104 (2010); doi:10.1016/j.ejrad.2009.03.057
7. E. E. Connor, J. Mwamuka, A. Gole, C. J. Murphy, and M. D. Wyatt, *NANO·MICRO Small*, **1**, Iss. 3: 325 (2005); doi:10.1002/smll.200400093
8. A. Jakhmola, N. Anton, and T. F. Vandamme, *Advanced Healthcare Materials*, **1**, Iss. 4: 413 (2012); doi:10.1002/adhm.201200032
9. O. Rabin, J. Manuel Perez, J. Grimm, G. Wojtkiewicz, and R. Weissleder, *Nature Mater.*, **5**, No. 2: 118 (2006); doi:10.1038/nmat1571
10. D. Pan, E. Roessl, J. P. Schlomka, S. D. Caruthers, A. Senpan, M. J. Scott, J. S. Allen, H. Zhang, G. Hu, and P. J. Gaffney, *Angewandte Chemie [International Ed. in English]*, **49**, No. 50: 9635 (2010); doi:10.1002/anie.201005657
11. J. A. Nadel, W. G. Wolfe, P. D. Graf, J. E. Youker, N. Zamel, J. H. Austin, W. A. Hinchcliffe, R. H. Greenspan, and R. R. Wright, *New Engl. J. Med.*, **283**: No. 6: 281 (1970); doi:10.1056/nejm197008062830603
12. S. Chakravarty, J. M. L. Hix, K. A. Wiewiora, M. C. Volk, E. Kenyon, D. D. Shuboni-Mulligan, B. Blanco-Fernandez, M. Kiupel, J. Thomas, L. F. Sempere, and E. M. Shapiro, *Nanoscale*, **12**, No. 14: 7720 (2020); doi:10.1039/d0nr01234c
13. H. Xing, W. Bu, Q. Ren, X. Zheng, M. Li, S. Zhang, H. Qu, Z. Wang, Y. Hua, K. Zhao, L. Zhou, W. Peng, and J. Shi, *Biomaterials*, **33**, Iss. 21: 5384 (2012); doi:10.1016/j.biomaterials.2012.04.002
14. S. Jafari, B. Mahyad, H. Hashemzadeh, S. Janfaza, T. Gholikhani, and L.

Tayebi, *Int. J. Nanomedicine*, **15**, 3447 (2020); doi:10.2147/ijn.s249441

15. H. E. Townley, E. Rapa, G. Wakefield, and P. J. Dobson, *Nanomedicine: Nanotechnology, Biology and Medicine*, **8**, Iss. 4: 526 (2012); doi:10.1016/j.nano.2011.08.003
16. X. Michalet, F. F. Pinaud, L. A. Bentolila, J. M. Tsay, S. Doose, J. J. Li, G. Sundaresan, A. M. Wu, S. S. Gambhir, and S. Weiss, *Science*, **307**, No. 5709: 538 (2005); doi:10.1126/science.1104274
17. A. Koudrina and M.C. DeRosa, *ACS Omega*, **5**, Iss. 36: 22691 (2020); doi:10.1021/acsomega.0c02650
18. H. M. Fahmy, A. M. Mosleh, A. A. Elghany, E. Shams-Eldin, E. S. Abu Serea, S. A. Ali, and A. E. Shalan, *RSC Advances*, **9**, 35: 20118 (2019); doi:10.1039/c9ra02907a
19. R. Abo Gabal, S. Osama, N. Hanafy, and A. Oraby, *Appl. Phys. A*, **129**, No. 3: 201-1 (2023); doi:10.1007/s00339-023-06482-8
20. J. Y. Park, P. Daksha, G. H. Lee, S. Woo, and Y. Chang, *Nanotechnology*, **19**, No. 36: 365603 (2008); doi:10.1088/0957-4484/19/36/365603
21. T. S. Gaaz, A. B. Sulong, M. N. Akhtar, A. A. Kadhum, A. B. Mohamad, and A A. Al-Amiery, *Molecules*, **20**, No. 12: 22833 (2015); doi:10.3390/molecules201219884
22. M. Babic, D. Horák, M. Trchová, P. Jendelová, K. Glogarová, P. Lesný, V. Herynek, M. Hájek, and E. Syková, *Bioconjug. Chem.*, **19**, Iss. 3: 740 (2008); doi:10.1021/bc700410z
23. S. S. Mano, K. Kanehira, S. Sonezaki, and A. Taniguchi, *Int. J. Mol. Sci.*, **13**, No. 3: 3703 (2012); doi:10.3390/ijms13033703
24. M. F. Vitha, *Spectroscopy. Principles and Instrumentation* (John Wiley & Sons: 2018).
25. M. Kannan, *Transmission Electron Microscope: Principle, Components and Applications Illumination System (Electron Gun and Condenser Lenses) Electron Gun*. In: *A Textbook on Fundamentals and Applications of Nanotechnology* (New Delhi: Daya Publishing House® A Division of Astral International Pvt. Ltd.: 2018), pp. 93–101.
26. G. V. Franks, *Journal of Colloid and Interface Science*, **249**, Iss. 1: 44 (2002); doi:10.1006/jcis.2002.8250
27. I. De Dios, L. Ramudo, J. R. Alonso, J. S. Recio, A. C. Garcia-Montero, and M. A. Manso, *FEBS Lett.*, **579**, Iss. 28: 6355 (2005); doi:10.1016/j.febslet.2005.10.017
28. R. A. Gabal, D. Shokeir, and A. Orabi, *Trends in Sciences*, **19**, No. 3: 2062 (2022); doi:10.48048/tis.2022.2062
29. E. M. Pogson, J. McNamara, P. Metcalfe, and R. A. Lewis, *Quantitative Imaging in Medicine and Surgery*, **3**, No. 1: 18 (2013); doi:10.3978/j.issn.2223-4292.2013.02.05